Analysis of structure and vibrational dynamics of the BeTe(001) surface using x-ray diffraction, Raman spectroscopy, and density functional theory

C. Kumpf,* A. Müller, W. Weigand, and E. Umbach
Lehrstuhl für Experimentelle Physik II, Universität Würzburg, D-97074 Würzburg, Germany

J. Wagner, V. Wagner, S. Gundel, L. Hansen, and J. Geurts
Lehrstuhl für Experimentelle Physik III, Universität Würzburg, D-97074 Würzburg, Germany

O. Bunk
Materials Research Department, Risø National Laboratory, DK-4000 Roskilde, Denmark

J. H. Zeysing, F. Wu, and R. L. Johnson
Institut für Experimentalphysik, Universität Hamburg, D-22761 Hamburg, Germany
(Received 18 March 2003; published 31 July 2003)

The atomic structure and lattice dynamics of epitaxial BeTe(001) thin films are derived from surface x-ray diffraction and Raman spectroscopy. On the Te-rich BeTe(001) surface $[1\bar{1}0]$-oriented Te dimers are identified. They cause a (2×1) superstructure and induce a pronounced buckling in the underlying Te layer. The Be-rich surface exhibits a (4×1) periodicity with alternating Te dimers and Te-Be-Te trimers. A vibration eigenfrequency of 165 cm^{-1} is observed for the Te-rich surface, while eigenmodes at 157 and 188 cm^{-1} are found for the Be-rich surface. The experimentally derived atomic geometry and the vibration modes are in very good agreement with the results of density functional theory calculations.

DOI: 10.1103/PhysRevB.68.035339 PACS number(s): 68.35.Bs, 68.35.Ja, 61.10.Nz, 78.30.Fs

I. INTRODUCTION

Epitaxial thin-film growth has become a key technology for fabricating semiconductor-based electronic and optoelectronic devices. Atomic layer by layer deposition is achieved in the molecular beam epitaxy (MBE) process by monitoring and controlling the growth parameters; for example, the substrate temperature and the particle flux in the molecular beams are of crucial importance. However, in order to understand the growth scenario and optimize device fabrication a detailed knowledge of the atomic arrangement at the surface is necessary. With this information it becomes possible to carry out computer simulations and model the growth process. Diffraction techniques are generally employed to reveal the periodic geometrical structure of surfaces and interfaces. Here we make use of x-ray diffraction with synchrotron radiation because it is particularly a direct and powerful technique. Raman spectroscopy provides unique insights into the local atomic arrangement and the associated atomic force constants. Recent advances in computing machinery and software have made feasible first-principle calculations to predict both the surface atomic geometry and surface dynamical properties of compound semiconductors. In this paper we employ all three methods to elucidate the BeTe(001) structure.

The samples we have investigated are BeTe epilayers grown on GaAs(001) wafers. BeTe is a wide band-gap II-VI compound. II-VI semiconductors in general are interesting for electro-optical applications and have been the object of several investigations over the past ten years.[1–4] Recently the incorporation of manganese atoms as isoelectronic magnetic dipoles has triggered new interest in these systems for spintronics applications.[5–8] Beryllium teluride is unique among II-VI compounds and exhibits unusual electronic, vibrational, and elastic properties. It has a large band gap (4.2 eV),[9] a high p dopability,[10] the lowest ionicity of all II-VI compounds, and a very high shear modulus.[11] The extreme mass asymmetry in the compound leads to a very specific and unusual phonon dispersion.[12] Furthermore, the lattice mismatch to GaAs and ZnSe is very small, which permits high quality epitaxial growth of heterostructures and superlattices. High film quality and defect-free interfaces are essential for achieving injection of totally spin-polarized electrons into nonmagnetic semiconductors (see Refs. 5–7 and references therein).

II. EXPERIMENTAL AND THEORETICAL METHODS

A. Sample preparation

The samples were prepared at Würzburg University in a Riber MBE System using standard techniques. The BeTe layer was deposited at a substrate temperature of 350 °C on a freshly grown, undoped GaAs buffer layer (thickness 40 nm). To avoid defects arising from film relaxation the BeTe layer thickness was typically less than 25 nm, i.e., well below the critical thickness for pseudomorphic growth. During growth, the partial pressure of Te was 1.1×10^{-6} mbar and the partial pressure of Be was only 2.6×10^{-8} mbar which limited the BeTe growth rate to 0.4 Å per second. Reflection high-energy electron diffraction (RHEED) monitoring of the growth process revealed the presence of a weak (2×1) reconstruction during growth. In the last stage of sample preparation the growth parameters were modified to yield either a Te-rich or a Be-rich surface. Te-rich surfaces were achieved by maintaining the Be and Te pressure constant

until the end of growth. The Be flux was then turned off, and the sample was cooled while maintaining the Te pressure at 1.1×10^{-6} mbar. In contrast, Be-rich surfaces were obtained by gradually reducing the Te pressure down to 1.5×10^{-7} mbar (i.e., a reduction by a factor of 7) before terminating the growth process by removing the Be flux.

When transporting the samples between the MBE growth system and the experimental stations for the Raman and surface x-ray diffraction investigations the samples were either kept under ultrahigh vacuum conditions (typically 3×10^{-10} mbar) or protected by a two-layer cap and a nitrogen atmosphere. The two-layer cap consisted of an amorphous Se layer on top of an amorphous Te layer, both nominally 100 nm thick. The cap layers were thermally desorbed prior to the Raman and x-ray studies by raising the sample temperature stepwise to 280 °C while monitoring the low-energy election diffraction (LEED) pattern. Both transport methods resulted in samples with clear and sharp LEED spots.

B. Surface x-ray diffraction

The surface x-ray diffraction (SXRD) measurements were performed on the *z*-axis diffractometer at the BW2 wiggler beamline at HASYLAB using an x-ray wavelength of 1.305 Å. After aligning the surface of the sample with respect to the incident x-ray beam, the angle of grazing incidence was set to 0.2°. For the (2×1) reconstructed Te-rich surface, a full in-plane data set and several fractional order and integer order Bragg rods were measured. The intensity of each reflection was determined by rotating the sample about its surface normal (ω scans). The peaks were integrated, background subtracted, and corrected for Lorentz and polarization factors, active sample area, and rod intercept in the standard manner as described in Refs. 13 and 14. Since the zinc-blende (001) surface has only twofold symmetry there is only one rotational domain and the diffraction pattern had *p2mm* symmetry. By averaging symmetry-equivalent reflections a systematic error in $|F|^2$ of $\epsilon=22\%$ was determined for the in-plane data set. The relatively high value can be attributed to the fact that the measurements were performed at an incidence angle of 0.2°, which is close to the critical angle of BeTe. The diffracted signal is enhanced at the critical angle which helps to compensate for the relatively low intensity of the BeTe superstructure reflections but the sample positioning also becomes more critical. The final data set consisted of 28 inequivalent in-plane reflections, eight fractional-order rods with 258 reflections, and two crystal truncation rods (CTR's) with 60 reflections. For fitting the data we used the code "fit."[15] Standard LEED coordinates ($\mathbf{a}=1/2[1\bar{1}0]_{\mathrm{bulk}}$, $\mathbf{b}=1/2[110]_{\mathrm{bulk}}$, $\mathbf{c}=[001]_{\mathrm{bulk}}$) are used in the following. Note that the thickness of the BeTe film was below the critical thickness for pseudomorphic growth, so the BeTe unit cell is slightly distorted. An exact evaluation of the positions of the (020) and the (011) Bragg reflections [corresponding to (220) and (111) in bulk units, respectively] yielded $|\mathbf{a}|=|\mathbf{b}|=4.002$ Å $\approx(1/\sqrt{2})a_{\mathrm{GaAs}}$ and $|\mathbf{c}|=5.583$ Å.

C. Raman spectroscopy

The Raman spectroscopy investigations of BeTe surface vibration eigenmodes were performed in a specially designed UHV-optics chamber, equipped with a docking station and a reentrant viewport for efficiently collecting the scattered light. Experimental details are described in more detail elsewhere,[16] while more general considerations on UHV-Raman experiments can be found in Refs. 17 and 18. The Raman spectra were recorded in a quasibackscattering geometry using the 476.5-nm laser line of an Ar^+-ion laser for excitation with an incident power of 80 mW focused to a spot diameter of 300 μm. The polarization vectors of the incident and scattered light were aligned with the principal axes of the surface, i.e., $[1\bar{1}0]$ and $[110]$. In Porto-notation[19] the configurations were $00\bar{1}(1\bar{1}0,1\bar{1}0)001$, $00\bar{1}(1\bar{1}0,110)001$, and $00\bar{1}(110,110)001$. The Raman scattered light was collected by an objective lens system with a numerical aperture of 1:3, analyzed by a SPEX 1403 double monochromator ($f=85$ cm) and detected with a GaAs photomultiplier in photon counting mode. The samples were cooled to 80 K in order to reduce the thermal broadening of the phonon peaks and to suppress the GaAs substrate multiphonon structures, e.g., 2TA(X) at 160 cm^{-1}, which might obscure the BeTe surface vibrational modes.

D. Density functional theory

First-principles calculations, applying density functional theory (DFT) within the local density approximation (LDA) were used to calculate the surface equilibrium configuration and the corresponding surface vibration modes. We used the fhi96md (Ref. 20) program code with norm-conserving pseudopotentials. The basis set of the electronic states consisted of plane waves with a kinetic energy cutoff of 163.2 eV (12 Rydberg) and a 2×1 supercell. The supercell consisted of a Te dimer layer on top of four bulk bi-layers of BeTe and was extended in the normal direction above the surface by 24 Å vacuum. The back side of the crystal was H terminated with a charge of $Z=0.5$ in order to avoid dangling bonds. A cubic unit cell with a lattice constant of $a_{lattice}=5.576$ Å $(=10.54a_{Bohr})$ was used. The surface was allowed to relax to the minimum-energy configuration with only the atoms in the lowest BeTe monolayer constrained to remain on bulk lattice sites.

In the second stage the surface vibration modes were calculated for the DFT-derived structure, using the frozen phonon approximation.[21] Starting from the equilibrium configuration, the Te atoms in the surface dimers were symmetrically displaced along the dimer axis. Subsequently displacement patterns of the bulk atoms were generated, according to the resulting forces on all atoms in the slab. This leads to a successive creation of the eigenmode pattern. The calculated forces, induced by the various displacement patterns, together with atomic masses were used to set up the dynamical matrix of the system within the harmonic approximation. Finally, the vibrational frequencies were obtained as the eigenvalues ω^2 of this dynamical matrix, while the eigenvectors gave the related displacement pattern of the mode.

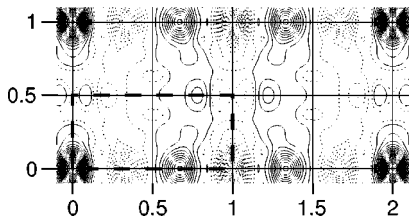

FIG. 1. Contour plot of the Patterson map calculated from the measured in-plane data set. One complete (2×1) unit cell is shown. The axes are scaled in LEED units ($|\mathbf{a}|=4.0020$ Å). Positive (negative) values are plotted as solid (dotted) contour lines. A thick dashed line indicates the irreducible unit.

III. RESULTS AND DISCUSSION

A. Surface structure

When evaluating surface x-ray-diffraction data it frequently turns out that finding a good starting model for the least-squares refinement is a crucial step. A good starting model should be sufficiently close to the correct solution that the refinement algorithm will converge rapidly and not get trapped in a subsidiary minimum. A useful initial step is to determine the interatomic vectors projected on the surface plane by calculating the two-dimensional Patterson function,

$$P(x,y)\propto\sum_{h,k}|F_{hk0}|^2\cos[2\pi(hx+ky)], \qquad (1)$$

where $|F_{hk0}|^2$ is the measured intensity of the in-plane reflections $(hk0)$. A Patterson contour plot calculated from the BeTe data is shown in Fig. 1. Positive peaks in the map, indicated by solid contour lines, identify interatomic distance vectors in the unit cell projected onto the surface plane.[22] The irreducible unit contains only one distinct peak at (0.66, 0), corresponding to a distance vector with a length of 2.63 Å, close to the Te-Te covalent bond length of 2.7 Å. Thus we can immediately conclude from the Patterson function that Te dimers oriented along the $[1\bar{1}0]$ direction are present on the surface. The small size of the unit cell and the *p2mm* symmetry means that there is only one way to position the Te dimer in the unit cell. Thus the atomic arrangement for the starting model is now fixed and consists of one Te dimer—centered in the (2×1) unit cell—on top of a Be-terminated bulk crystal. In the following we discuss the least-squares refinement performed with this starting model.

In a first iteration the positions of the Te dimer and the atoms in the two uppermost BeTe bilayers were refined. This yielded $\chi^2=2.69$ for the whole data set, however, the in-plane data and the fractional order rods yielded better fit results than the integer order rods as discussed below. As this was consistently observed in several trials we decided to exclude the integer-order data from the subsequent structural refinement. Using only the fractional-order data $\chi^2=1.47$ was obtained for a model with the same set of parameters. Next the occupation of the atomic sites in the surface region was investigated and it was found that all sites were occupied. Variation of the Debye-Waller factors revealed that three different Debye-Waller factors were necessary to fit the data, one for the Te dimers and one for each atomic species in the uppermost bulklike layer. All other Debye-Waller factors were fixed at bulk values. Several fits were performed using these constraints to optimize the positions of different numbers of BeTe bulk layers. Models with two and three bilayers fitted the experimental data almost equally well ($\chi^2=1.18$ and 1.14, respectively). Refining the positions of more than three bulk bilayers produced an increase in χ^2 due to the increase in the number of fit parameters. It should be noted that because of the small atomic scattering factor of Be compared to Te, to ensure physically reasonable sites for the Be atoms, it was necessary to include the Keating energy[23,24] as an additional constraint in the fit procedure. A penalty was added to the goodness-of-fit (GOF) function proportional to the deviation of the squared BeTe bond length from the ''ideal'' covalent bond length of 2.436 Å. The Keating term was only applied to bulklike Be-Te bonds and not to the Te-Te surface dimers and was needed to constrain the BeTe bond lengths to reasonable values. In this way it was possible to avoid unphysical coordinates for the Be atoms which would have falsified the positions of the surface Te atoms. In summary, for the final fit shown in Fig. 2, 14 positional parameters (the Te dimer and three BeTe bilayers), three Debye-Waller factors, and two scaling parameters were adjusted. The fit parameters are listed in Table I and the corresponding atomic model is shown in Fig. 3.

As indicated above we could not fit the measured crystal truncation rods using the Te dimer model. The solid line in Fig. 2(c) shows the intensity variation calculated using our final model, but the dashed lines in the figure demonstrate that the measured intensities are much closer to a $\sin^{-2}(\frac{1}{2}\pi l)$-dependence which is expected for the (hkl) rods with even h and k for an unreconstructed surface. Disordered areas on the surface would also generate a similar l dependence for the intensities along integer-order rods. The result suggests that this particular BeTe(001) surface contains (2×1) reconstructed domains for which the model developed here is valid, and additional unreconstructed areas which do not contribute to the fractional-order reflections. The shape of the CTR's, in particular their slope near the bulk Bragg points, indicates that the intensity difference in the CTR's is not simply due to surface roughness, but mostly to disordered or unreconstructed areas. To ensure that the model developed in this paper is not misled by an inhomogeneous sample, all integer order data were omitted from the quantitative analysis of the surface structure. Usually the data are needed to determine the registry of the adsorbate relative to the substrate, but for BeTe(001) the relative position of adsorbate and subtrate atoms is obvious from the bond chemistry and constrained by the stepwise relaxation of the atoms towards their bulklike positions in underlying layers.

Our DFT calculations of the Te rich BeTe(001) surface also yield a (2×1) reconstruction, the dominant structural features of which are symmetric Te dimers located 1.4 Å above the underlying Be plane. The dimers are oriented along the $[1\bar{1}0]$ direction and arrange themselves in one-dimensional rows. The occurrence of symmetrical dimers is quite common for (2×1)-reconstructed II-VI (001) surfaces.[25,26] In Table I detailed atomic positions derived

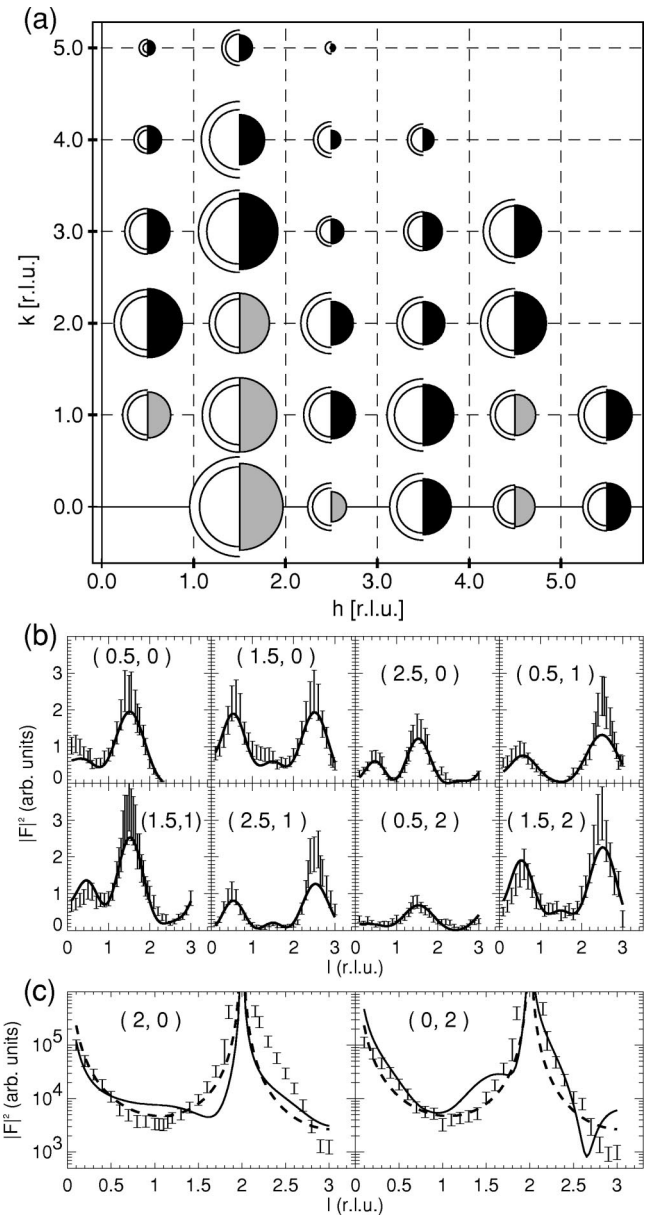

FIG. 2. (a) Plot of the in-plane data. The areas of the open and filled semicircles represent measured and calculated intensities, respectively. Two open semicircles indicate the error range in the experimental data. Gray/white circles have been scaled by a factor of 0.5 with respect to the black/white circles. (b) Fractional and (c) integer order rods. Error bars represent the measured data, solid lines are calculated using the best fitting model (see Fig. 3 and Table I). The dashed lines in (c) are calculated for an ideal, unreconstructed BeTe surface (see text).

from the DFT calculations are listed and compared with the SXRD results. The dimer distance, evaluated by DFT is 2.81 Å, compared to the value found in the SXRD experiment of 2.778(6) Å. Both values are in very good agreement with each other and are also consistent with the value of twice the covalent radius of Te (2.80 Å). Another important feature in the structure is the extreme vertical buckling of the Te atoms in the topmost bulklike layer. The SXRD refinement yielded a height difference of $\Delta = 0.395(9)$ Å between the atoms Te-1 and Te-2 (see Fig. 3), which again is in good agreement with the value found in the DFT calculations (0.41 Å). This buckling is caused by a strong outward relaxation [0.248(6) Å] of the Te-1 atoms lying between the dimer rows and a smaller inward shift of the Te-2 atoms located below the Te dimer rows [$-0.147(7)$ Å from their bulk positions]. The interaction between the buckling effect in the first bulk layer and the dimerization in the adlayer is mediated by the Be-1 atoms lying between the Te dimers and the Te-2 atoms. These atoms exhibit a lateral relaxation of 0.16(7) Å in the direction towards the center of the unit cell.

These strain-induced relaxation effects proceed into deeper layers with a decreasing amplitude, but they can still be detected in the third Te bulk-layer as indicated by a 0.030(7) Å difference in height between the Te-4 and Te-5 atoms. Small arrows in Fig. 3(c) illustrate the displacements: The atoms in the sequence of BeTe bilayers are shifted alternately in lateral and vertical directions which enables the strain induced by the surface dimers to be relaxed in the three uppermost bulk layers.

We believe that the lateral relaxation of the Be-1 atoms is the reason for the linear arrangement of the Te-dimer rows which results in the (2×1) superstructure. The alternative one might think about, namely the formation of a $c(2\times2)$ superstructure with alternating dimers, means that every second dimer in the row would be shifted by $(1,0)_{\mathrm{LEED}}$, half of the unit cell in $[1\bar{1}0]_{\mathrm{bulk}}$ direction. This would inhibit any lateral relaxation of the Be-1 atoms due to the *c2mm* symmetry of that unit cell. [In a $c(2\times2)$ unit cell the Be-1 atoms lie on the intersection point of two glide planes.] This means that the buckling of the Te-2 and -3 atoms would also be inhibited and the upper bulk layers would not be able to accommodate the strain induced by the dimerized adlayer.

B. Vibrational dynamics

Figure 4(a) shows Raman spectra from a clean Te-rich (2×1) reconstructed surface for three different polarization configurations. The polarization directions of the incident and scattered light are indicated by the E_i and E_s arrows. The strongest spectral features are the optical-phonon peaks from the GaAs substrate at 294 cm^{-1} (GaAs-LO) and 271 cm^{-1} (GaAs-TO). Since the BeTe bulk TO and LO frequencies are 462 and 502 cm^{-1}, as obtained from infrared and Raman spectroscopy,[12] they are not included in Fig. 4(a).

An additional feature is observed at 165 cm^{-1} only when both E_i and E_s polarizations are along the $[1\bar{1}0]$ direction. This nonequivalence of the [110] and $[1\bar{1}0]$ directions is inconsistent with the symmetry of the zinc-blende bulk structure of BeTe and GaAs and indicates that the peak is due to a surface or interface vibrational mode. The Raman spectra from a sample with a Be-rich surface, shown in Fig. 4(b), has two peaks which appear at 157 and 188 cm^{-1}. There is a clear dependence on the surface termination of the sample, and hence we can assign these features to surface-related modes. The polarization dependence is the same as for the Te-rich surface. In the following we consider the symmetry selection rules for Raman scattering from reconstructed BeTe(001) surfaces.

TABLE I. Atomic parameters for the (001)-(2×1) reconstruction of BeTe determined by SXRD and DFT. Isotropic Debye-Waller (DW) factors determined from the SXRD data are listed in column 2. Values missing in the table were fixed at their bulk values (0.80 Å^2 for Be and 2.43 Å^2 for Te). In columns 3 and 4 the atomic positions (SXRD results) are given in LEED coordinates and Å, respectively. The standard deviations listed in these columns were calculated assuming uncorrelated parameters. Values listed without error were not refined due to the *p2mm* symmetry constraints. For the Be atoms relatively large errors were determined since no Keating-energy constraints were used for the error determination. In column 5 the results of the DFT calculations are listed, and column 6 contains the deviations between the results of both methods (in LEED units).

Site	DW in Å^2	SXRD results: Positions (x,y,z)	SXRD results: Positions in Å [a]	DFT results: Positions (x,z) [b]	Deviation SXRD-DFT (x,z)
Te-*d*	2.94(8)	(0.651(1), 0.5, 0.267(1))	(2.604(4), 2.001, 1.209(7))	(0.643, 0.274)	(0.008, −0.007)
Be1	1.3(9)	(0.54(2), 0.0, 0.02(4))	(2.16(7), 0.000, −0.18(22))	(0.550, 0.020)	(−0.010, −0.002)
Te1	1.0(2)	(0.0, 0.0, −0.206(1))	(0.000, 0.000, −1.430(6))	(0.0, −0.195)	(0, −0.011)
Te2	1.0(2)	(1.0, 0.0, −0.276(1))	(4.002, 0.000, −1.825(7))	(1.0, −0.269)	(0, −0.007)
Be2		(0.0, 0.5, −0.45(4))	(0.000, 2.001, −2.78(20))	(0.0, −0.461)	(0, 0.012)
Be3		(1.0, 0.5, −0.50(2))	(4.002, 2.001, −3.08(10))	(1.0, −0.510)	(0, 0.008)
Te3		(0.479(1), 0.5, −0.719(4))	(1.918(3), 2.001, −4.28(2))	(0.483, −0.739)	(−0.004, 0.020)
Be4		(0.50(1), 0.0, −0.98(8))	(2.00(4), 0.000, −5.64(45))	(0.492, −0.993)	(0.011, 0.014)
Te4		(0.0, 0.0, −1.243(1))	(0.000, 0.000, −7.012(7))	(0.0, −1.250)	(0, 0.007)
Te5		(1.0, 0.0, −1.237(1))	(4.002, 0.000, −6.982(7))	(1.0, −1.242)	(0, 0.005)

[a]For the conversion from "LEED" to Å units pseudomorphically distorted surface lattice units, i.e., those of the GaAs[110] surface were used (see end of Sec. II B).

[b]y is fixed due to the symmetry of the unit cell, and therefore identical to the number given in column 3.

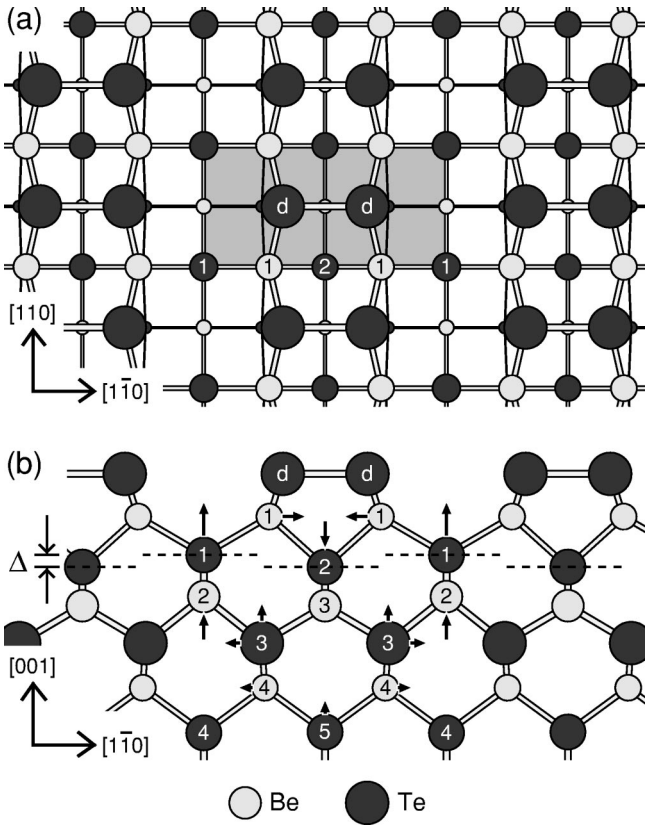

FIG. 3. Structural model for the BeTe(001)-(2×1) surface viewed from (a) above and (b) from the side. Be and Te atoms are shown as light gray and black circles. Gray bars represent covalent bonds. In (a) the (2×1) unit cell is indicated by a gray area. Small arrows in (b) indicate the direction of relaxation of the atoms.

The (2×1) reconstructed (001) surface of a zinc-blende crystal in general has the symmetry point group C_s. A dimer stretching vibration has the A' symmetry, which is described by the Raman tensor

$$\begin{pmatrix} a & 0 & 0 \\ 0 & b & d \\ 0 & d & c \end{pmatrix}. \qquad (2)$$

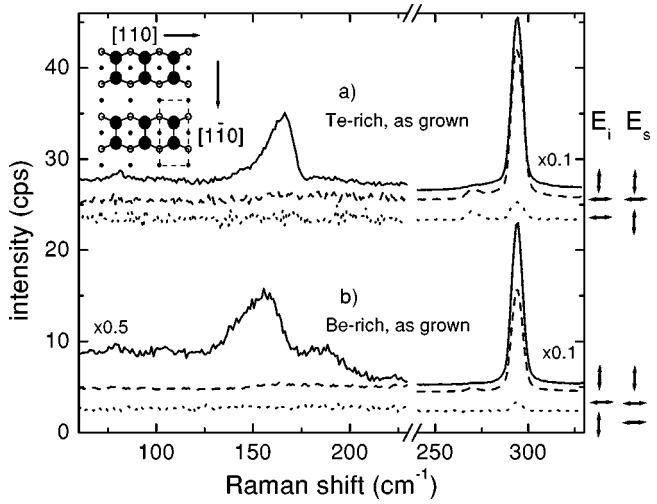

FIG. 4. UHV-Raman spectra of BeTe/GaAs(001) heterostructures for (a) the Te-rich surface and (b) the Be-rich BeTe surface. For each spectrum the arrows indicate the polarization directions of the incident and scattered light with respect to the principal surface axes, as shown in the inset. The wavelength of the laser was 476.5 nm, the sample temperature 80 K.

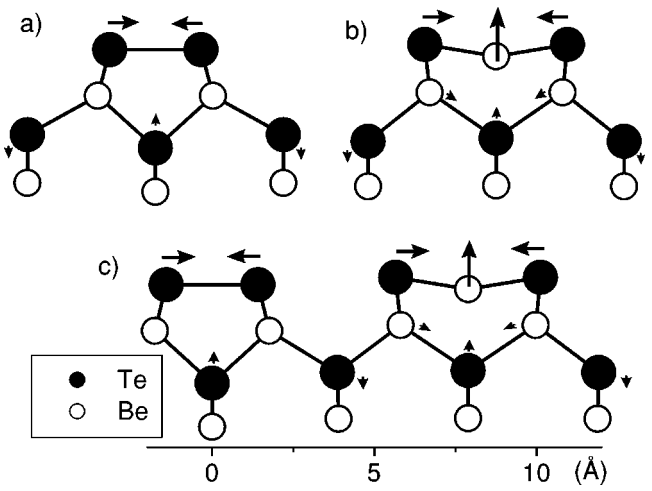

FIG. 5. Vibrational eigenmodes of BeTe(001) surfaces, derived from density functional theory calculations. A view along the [110] direction is shown for (a) a Te-rich (2×1) surface with Te dimers, (b) a Be-rich (2×1) surface with Te-Be-Te trimers, and (c) a Be-rich surface with alternating Te-Be-Te trimers and Te dimers. The arrows indicate the atomic displacement patterns, derived from frozen phonon calculations.

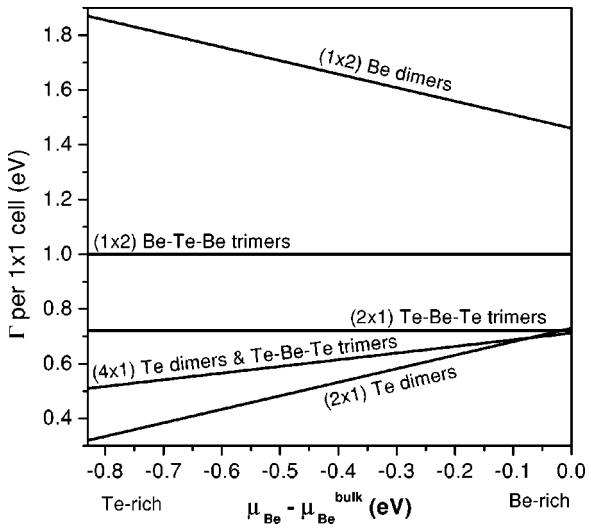

FIG. 6. DFT-derived surface excess energies Γ for different configurations of Te and Be dimers as well as Be-Te-Be and Te-Be-Te trimers, plotted vs the chemical potential.

Symmetric (i.e., in-plane) dimers produce a higher symmetry surface with C_{2v} point group and A_1 symmetry for the symmetric-dimer stretching vibration. This means that the component d of the Raman tensor becomes zero. The experimental data in Fig. 4 yield a finite value for c, but b and d are zero. These observations are consistent with symmetric dimers ($d=0$), the polarizability of which is large along the dimer axis $[1\bar{1}0]$ (finite c) and nearly zero perpendicular to the dimer axis ($b\approx0$). The symmetry characteristics of our Raman spectra are entirely consistent with the surface geometry derived from the SXRD and DFT results.

By comparing the frequencies of the surface vibrational modes derived from the DFT calculations with the observed Raman lines we were able to uniquely identify the lines. For the Te-rich (2×1) surface, the DFT-derived Te-dimer vibration pattern is indicated by the arrows in Fig. 5(a). For this eigenmode, the LDA calculation yields a frequency of 166.8 cm^{-1}, which is in excellent agreement (within 1.1%) with the experimental finding of 165 cm^{-1} and confirms our peak assignment. This strongly supports the correctness of the BeTe(001)-(2×1) model for the Te-rich surface presented here.

The Raman spectra from the Be-rich surface reveal two peaks located at 157 and 188 cm^{-1}, as shown in Fig. 4(b). These peaks cannot be explained by merely substituting Be dimers for the Te dimers because the lighter Be dimers would have a significantly higher frequency in the region of 600 cm^{-1}. In the literature a (4×1) reconstruction has been reported for the Be-rich surface,[27,28] which may be accompanied by a transition between (4×1) and (3×1) phases.[28] We chose a series of candidate surface configurations, based on a well established set of II-VI-surface structures,[29] and calculated their surface excess energies using the DFT method. Our DFT calculations covered the whole chemical potential range from Te-rich to Be-rich surfaces. The candidate configurations consisted of Te dimers (2×1), Be dimers (1×2), Be-Te-Be trimers (1×2), Te-Be-Te trimers (2×1), and a configuration consisting of alternate Te dimers and Te-Be-Te trimers (4×1). The DFT-calculated surface excess energy values of these configurations are plotted in Fig. 6. Clear trends are visible for the Te dimers and the Be dimers. As expected, the Te dimers on Te-rich surfaces have the lowest excess energy. They constitute the most stable configuration and, furthermore, their excess energy increases with increasing Be content. Similarly, the Be-dimer excess energy decreases with increasing Be content, but it remains significantly higher than the other candidates. The trimer configurations yield nearly constant energies, while the (4×1) configuration with alternating dimers and trimers shows an intermediate dependence on the Te/Be ratio. We were surprised to find for the Be-rich surface that the three possible configurations all had rather similar excess energies. The DFT calculations clearly rule out Be dimers on the surface and make Be-Te-Be trimers less likely, but cannot unambiguously guide us to a single surface configuration.

As a next step we calculated the vibrational frequencies of Te-Be-Te trimers, and alternate Te-Be-Te trimers and Te dimers, following the procedure described above for the Te dimers on the (2×1) surface. A configuration consisting of consecutive Te-Be-Te trimers, as shown in Fig. 5(b), results in a single vibration mode with a frequency of 210.0 cm^{-1}, which clearly does not agree with our experimental Raman data. The arrangement with alternating Te-Be-Te trimers and Te-Te-dimers, as depicted in Fig. 5(c), produces two surface modes: a Te-dimer frequency of 159.7 cm^{-1} [slightly downshifted compared to Te dimers on a Te-rich (2×1) surface] and a Te-Be-Te-trimer frequency of 187.5 cm^{-1}. These frequencies are again in excellent agreement with the experimental results of 157 and 188 cm^{-1}. Thus our Raman results are fully consistent with the local atomic arrangement shown

in Fig. 5(c), which corresponds to a (4×1) surface reconstruction as reported in Refs. 27 and 28. On our samples we only observed a very weak (4×1) diffraction pattern in LEED. We attribute this to a lack of sufficiently large coherent regions on the sample surface and this also hampered our SXRD experiments on the Be-rich surfaces. Raman spectroscopy as a local probe yielded the essential information that was not obtainable via conventional diffraction techniques.

The formation of Te-Be-Te trimers may be understood as the incorporation of Be atoms, which break the Te-dimer bonds and locate themselves midway along the broken dimer bond. In the MBE process these Be atoms may act as nucleation centers that catch the incoming Te atoms which locate themselves above the Te-2 atoms. Here they find neighbors for forming dimers and can bond to Te atoms adsorbed above the Te-1 site, and in this way the growth of one BeTe bilayer can be completed. Thus our models for the atomic configurations of the Te-rich and the Be-rich surfaces are consistent with plausible scenarios for the BeTe growth process.

IV. SUMMARY

In summary, we derived a detailed model for the atomic configuration and lattice dynamics of the BeTe (001) surface. The model is based on SXRD, Raman spectroscopy, and DFT results. The Te-rich BeTe(001) surface has a (2×1) reconstruction, with symmetric Te dimers along the $[1\bar{1}0]$ direction. The strain relaxation in the topmost layer leads to concomitant strain relaxation in the underlying layers and induces a sequence of alternating lateral and vertical shifts in successive BeTe bi-layers. In contrast, the Be-rich surface tends to form a (4×1) reconstruction consisting of alternating Te dimers and Te-Be-Te trimers oriented in the $[1\bar{1}0]$ direction. Characteristic surface vibrational eigenmodes were observed in Raman spectroscopy for light polarized along the axis of the dimers or trimers. Their eigenfrequencies agree within 1% with the values calculated from density functional theory. The atomic configurations suggest plausible models for the growth of BeTe thin films with molecular beam epitaxy.

ACKNOWLEDGMENTS

We thank the HASYLAB staff for technical assistance. This work was supported by the Deutsche Forschungsgemeinschaft through Sonderforschungsbereich 410 (TB B1), and the IHP program ''Access to Research Infrastructures'' of the European Commission (HPRI-CT-1999-00040). One of us (O.B.) acknowledges financial support from the Danish Research Council through Dansync.

*Corresponding author. Electronic address: kumpf@physik.uni-wuerzburg.de

[1] K. Pinardi, U. Jain, S.C. Jain, H.E. Maes, R. Van Overstraeten, and M. Willander, J. Appl. Phys. **83**, 4724 (1998).

[2] M.A. Vidal, M.E. Constantino, B. Salazar-Herandez, H. Navarro-Contreras, M. Lopez-Lopez, I. Heranandez-Calderon, and H. Yonezu, Defect Diffus. Forum **173-174**, 31 (1999).

[3] H. Neureiter, S. Tatarenko, S. Spranger, and M. Sokolowski, Phys. Rev. B **62**, 2542 (2000); C. Heske, U. Winkler, D. Eich, R. Fink, E. Umbach, Ch. Jung, and P.R. Bressler, *ibid.* **56**, 13 335 (1997); L. Seehofer, G. Falkenberg, R.L. Johnson, V.H. Etgens, S. Tatarenko, D. Brun, and B. Daudin, Appl. Phys. Lett. **67**, 1680 (1995).

[4] W. Weigand, C. Kumpf, M. Sokolowski, A. Bader, C. Schumacher, A. Möginger, W. Faschinger, L.W. Molenkamp, and E. Umbach, Phys. Status Solidi B **229**, 117 (2002); Z.H. Chen, M. Sokolowski, F. Stadler, M. Schneider, R. Fink, and E. Umbach, Europhys. Lett. **59**, 552 (2002).

[5] R. Fiederling, M. Keim, G. Reuscher, W. Ossau, G. Schmidt, A. Waag, and L.W. Molenkamp, Nature (London) **402**, 787 (1999); P. Ball, *ibid.* **404**, 918 (2000).

[6] R. Fitzgerald, Phys. Today **53** (4), 41 (2000).

[7] J.J. Berry, S.H. Chun, K.C. Ku, N. Samarth, I. Malajovich, and D.D. Awschalom, Appl. Phys. Lett. **77**, 3812 (2000).

[8] Th. Gleim, L. Weinhardt, Th. Schmidt, R. Fink, C. Heske, E. Umbach, P. Grabs, G. Schmidt, L.W. Molenkamp, B. Richter, A. Fleszar, and H.-P. Steinrück, Appl. Phys. Lett. **81**, 3813 (2002).

[9] K. Wilmers, T. Wethkamp, N. Esser, C. Cobet, W. Richter, V. Wagner, A. Waag, H. Lugauer, F. Fischer, T. Gerhard, M. Keim, and M. Cardona, Phys. Status Solidi B **215**, 15 (1999).

[10] H.-J. Lugauer, F. Fischer, T. Litz, A. Waag, U. Zehnder, W. Ossau, T. Gerhard, G. Landwehr, C. Becker, R. Kruse, and J. Geurts, Mater. Sci. Eng., B **43**, 88 (1997).

[11] C. Verie, *Proceedings of the International Conference on Semiconductor Heteroepitaxy* (Montpellier, France, 1995), p. 73.

[12] V. Wagner, J.J. Liang, R. Kruse, S. Gundel, M. Keim, A. Waag, and J. Geurts, Phys. Status Solidi B **215**, 87 (1999).

[13] R. Feidenhans'l, Surf. Sci. Rep. **10**, 105 (1989).

[14] E. Vlieg, J. Appl. Crystallogr. **30**, 532 (1997).

[15] O. Bunk (unpublished).

[16] V. Wagner, J. Wagner, W. Faschinger, G. Bacher, J. Geurts, B. Schreder, and W. Kiefer, *Proceedings of the 17th International Conference on Raman Spectroscopy (ICORS2000)* (Beijing, China, 2000), p. 576.

[17] V. Wagner, D. Drews, N. Esser, D.R.T. Zahn, J. Geurts, and W. Richter, J. Appl. Phys. **75**, 7330 (1994).

[18] V. Wagner, W. Richter, J. Geurts, D. Drews, and D.R.T. Zahn, J. Raman Spectrosc. **27**, 265 (1996).

[19] T.C. Damen, S.P.S. Porto, and B. Tell, Phys. Rev. **142**, 570 (1966).

[20] M. Bockstedte, A. Kley, J. Neugebauer, and M. Scheffler, Comput. Phys. Commun. **107**, 187 (1997).

[21] J. Fritsch and U. Schröder, Prog. Theor. Phys. **309**, 209 (1999).

[22] Negative peaks are artefacts arising from the fact that only fractional-order in-plane data are used for calculating the Patterson function. Integer order reflections are skipped since they are superimposed by the bulk signal. Thus only atomic distances in the reconstructed surface regions are reflected by the Patterson function.

[23] P.N. Keating, Phys. Rev. **145**, 637 (1966).

[24] J.S. Pedersen, Surf. Sci. **210**, 238 (1989).

[25] C.H. Park and D.J. Chadi, Phys. Rev. B **49**, 16 467 (1994).

[26] S. Gundel, A. Fleszar, W. Faschinger, and W. Hanke, Phys. Rev. B **59**, 15 261 (1999).

[27] M.W. Cho, J.H. Chang, D.M. Bagnall, K.W. Koh, S. Saeki, K.T. Park, Z. Zhu, K. Hiraga, and T. Yao, J. Appl. Phys. **85**, 512 (1999); M.W. Cho, J.H. Chang, S. Saeki, S.Q. Wang, and T. Yao, J. Vac. Sci. Technol. A **18**, 457 (2000).

[28] E. Tournie, V. Bousquet, and J.P. Faurie, Appl. Phys. Lett. **72**, 2859 (1998).

[29] A. Garcia and J.E. Northrup, J. Vac. Sci. Technol. B **12**, 2678 (1994).